

Article

# Morphological Evolution of Vertically Standing Molybdenum Disulfide Nanosheets by Chemical Vapor Deposition

Song Zhang <sup>1,\*</sup> , Jiajia Liu <sup>1</sup>, Karla Hernandez Ruiz <sup>1</sup>, Rong Tu <sup>1,\*</sup>, Meijun Yang <sup>1</sup>, Qizhong Li <sup>2</sup>, Ji Shi <sup>1,3</sup>, Haiwen Li <sup>1,4</sup> , Lianmeng Zhang <sup>1</sup> and Takashi Goto <sup>5</sup>

<sup>1</sup> State Key Laboratory of Advanced Technology for Materials Synthesis and Processing, Wuhan University of Technology, Wuhan 430070, China; jiajiali@whut.edu.cn (J.L.); kaheeruz30@gmail.com (K.H.R.); liyangmeijun@163.com (M.Y.); li.haiwen.305@m.kyushu-u.ac.jp (H.L.); lmzhang@whut.edu.cn (L.Z.)

<sup>2</sup> Hubei Key Laboratory Advanced Technology of Automobile Parts, Wuhan University of Technology, Wuhan 430070, China; qizhongli@whut.edu.cn

<sup>3</sup> School of Materials and Chemical Technology, Tokyo Institute of Technology, Tokyo 152-8552, Japan; Shi.j.aa@m.titech.ac.jp

<sup>4</sup> International Research Center for Hydrogen Energy, Kyushu University, Fukuoka 819-0395, Japan

<sup>5</sup> Institute for Materials Research, Tohoku University, Sendai 980-8577, Japan; goto@imr.tohoku.ac.jp

\* Correspondence: superkobe0104@gmail.com (S.Z.); turong@whut.edu.cn (R.T.); Tel.: +86-27-8749-9449 (S.Z.); +86-27-8749-9449 (R.T.)

Received: 6 March 2018; Accepted: 17 April 2018; Published: 20 April 2018



**Abstract:** In this study, we demonstrated the chemical vapor deposition (CVD) of vertically standing molybdenum disulfide ( $\text{MoS}_2$ ) nanosheets, with an unconventional combination of molybdenum hexacarbonyl ( $\text{Mo}(\text{CO})_6$ ) and 1,2-ethanedithiol ( $\text{C}_2\text{H}_6\text{S}_2$ ) as the novel kind of Mo and S precursors respectively. The effect of the distance between the precursor's outlet and substrates (denoted as  $d$ ) on the growth characteristics of  $\text{MoS}_2$ , including surface morphology and nanosheet structure, was investigated. Meanwhile, the relationship between the structure characteristics of  $\text{MoS}_2$  nanosheets and their catalytic performance for hydrogen evolution reaction (HER) was elucidated. The formation of vertically standing nanosheets was analyzed and verified by means of an extrusion growth model. The crystallinity, average length, and average depth between peak and valley ( $R_z$ ) of  $\text{MoS}_2$  nanosheets differed depending on the spatial location of the substrate. Good crystallized  $\text{MoS}_2$  nanosheets grown at  $d = 5.5$  cm with the largest average length of 440 nm, and the highest  $R_z$  of 162 nm contributed to a better HER performance, with a respective Tafel slope and exchange current density of 138.9 mV/decade, and 22.6  $\mu\text{A}/\text{cm}^2$  for raw data (127.8 mV/decade and 19.3  $\mu\text{A}/\text{cm}^2$  for iR-corrected data).

**Keywords:**  $\text{MoS}_2$  nanosheets; chemical vapor deposition; hydrogen evolution reaction

## 1. Introduction

Chemical vapor deposition (CVD) is considered to be the most practicable technique for synthesizing large-area, high quality, and size and thickness controllable  $\text{MoS}_2$  with different morphologies [1], including nanotubes [2], nanowires [3], nanosheets [4–6], etc., which are related to the anisotropic structure of  $\text{MoS}_2$ . Vertically standing  $\text{MoS}_2$  nanosheets have aroused great interest from researchers due to their extensively exposed edge sites arising from a high-aspect-ratio nanostructure, which hold great potential for diverse applications such as hydrogen evolution reaction (HER) [7], hydrogen storage devices [8], lithium ion batteries [9], supercapacitors [10], and hydrodesulfurization catalysis [11], as well as for biological applications [12]. Both theoretical and experimental studies

have indicated that the sulfide-terminated Mo-edge sites of MoS<sub>2</sub> are catalytically active, while the basal plane remains inert [4,13–17]. Li found that larger, dense exposed edges of vertical MoS<sub>2</sub> sheets can lead to a more active HER electro-catalyst [15]. However, while extensive studies have been devoted to two-dimensional materials which lie flat on the substrates [18–21], few reports have been developed regarding the growth of vertically standing MoS<sub>2</sub> nanosheets [6,11,22–26]. The growth of such vertically standing nanosheets is still challengeable, and more efforts should be made to explore the growth characteristics of nanosheets. In previous studies, the distance between the precursor's outlet and substrates was found to be an important factor in the growth of MX<sub>2</sub> (M = Mo, W; X = S, Se, Te) [1,27,28]. Wang [21] proved that MoS<sub>2</sub> domains showed a regular morphology transformation and a size change with the increase in distance between the precursor's outlet and the substrate. Lin [29] found that domain size and surface coverage were varied dramatically by changing the distance between source and growth substrates. By optimizing the growth conditions, they grew a single-crystalline MoS<sub>2</sub> flake, larger than 300 μm in size. Therefore, tuning the source–substrate distance is a practical method of controlling the morphology and size of MoS<sub>2</sub> nanosheets.

As for the precursors of MoS<sub>2</sub> synthesis, molybdenum hexacarbonyl (Mo(CO)<sub>6</sub>) is commonly used as an Mo precursor to the growth of molybdenum compounds [30–32], including MoS<sub>2</sub>, as the melting point of Mo(CO)<sub>6</sub> is quite low, meaning only a low energy is required to evaporate it, and making it easily controllable when adding it to the reaction chamber. 1,2-ethanedithiol (SHCH<sub>2</sub>CH<sub>2</sub>SH, or C<sub>2</sub>H<sub>6</sub>S<sub>2</sub>), which remains in a liquid state at room temperature, is different to hydrogen sulfide (H<sub>2</sub>S) [30,31], and much less toxic than dimethyl disulfide (CH<sub>3</sub>SSCH<sub>3</sub>) [32–34], was adopted as an S precursor.

In this contribution, we provide a facile CVD method for depositing vertically standing MoS<sub>2</sub> nanosheets on diverse substrates, using Mo(CO)<sub>6</sub> and 1,2-ethanedithiol (C<sub>2</sub>H<sub>6</sub>S<sub>2</sub>) as the unconventional combination of precursors. MoS<sub>2</sub> nanosheets were grown at different substrate spatial locations (i.e., the distance between the precursor's outlet and the substrates, denoted as *d*). The effect of *d* on growth characteristics, and its relationship with catalytic performance were discussed.

## 2. Materials and Methods

Molybdenum hexacarbonyl (Mo(CO)<sub>6</sub>, 98.0%, Alfa Aesar, Shanghai, China) and 1,2-ethanedithiol (C<sub>2</sub>H<sub>6</sub>S<sub>2</sub>, 99.0%, TCI, Shanghai, China) were used as precursors for the growth of MoS<sub>2</sub> nanosheets. The experimental setup is illustrated in Figure 1. The substrates, fused quartz (10 × 10 × 0.5 mm<sup>3</sup>), were cleaned successively in acetone, isopropyl alcohol (IPA), and deionized (DI) water in an ultrasonic bath for 10 min, and then dried with an ultra high purity (UHP) N<sub>2</sub> stream. Mo(CO)<sub>6</sub> and C<sub>2</sub>H<sub>6</sub>S<sub>2</sub> were placed in vaporizers and maintained at 50 and 70 °C respectively. The vapor transport pipes were heated and kept at 80 °C. Ar and H<sub>2</sub> were used as carrier gas and reducing gas respectively. The substrate was placed on an alumina ceramic boat in the setting position of the tube, and the distance between the precursor's outlet and the substrates was denoted as *d* (as shown in Figure 1). The furnace was heated at a rate of 10 °C/min to 700 °C under a H<sub>2</sub> flow of 100 sccm. Following this, the H<sub>2</sub> flow rate was set to 500 sccm, while the total pressure (*P*<sub>tot</sub>) reached 250 Pa. 40 sccm of Ar gas was allowed through vaporizers to carry both Mo(CO)<sub>6</sub> and C<sub>2</sub>H<sub>6</sub>S<sub>2</sub> vapors respectively. Mo(CO)<sub>6</sub> and C<sub>2</sub>H<sub>6</sub>S<sub>2</sub> precursors were introduced into the reactor at 700 °C for 5 min. After deposition, the furnace was naturally cooled down to room temperature by a H<sub>2</sub> flow of 100 sccm at *P*<sub>tot</sub> = 100 Pa.

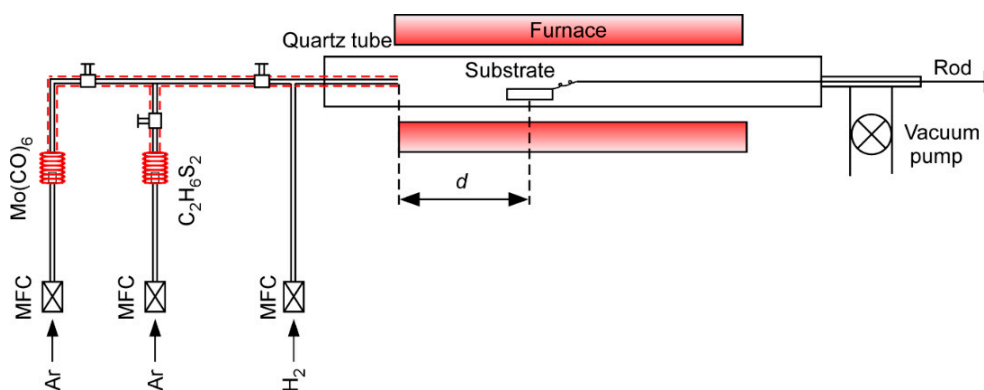


**Figure 1.** Schematic illustration of chemical vapor deposition (CVD) system.

X-ray diffraction microscopy (XRD; Ultima III, Rigaku, Tokyo, Japan, at 40 kV and 40 mA), Raman spectroscopy (Labram HR Evolution, Horiba, Kyoto, Japan, with a 532 nm laser) and Transmission electron microscopy (TEM; JEOLJEM-2100, Tokyo, Japan, at 200 kV) were used to characterize the microstructure of vertically standing MoS<sub>2</sub> nanosheets. A Field-emission scanning electron microscope (FESEM; Quanta-250, FEI, Houston, TX, USA, at 20 kV) and Atomic force microscopy (AFM; Veeco Nanoscope IIIa, Veeco, Plainview, NY, USA, tapping mode) were used to observe the surface morphology of vertically standing MoS<sub>2</sub> nanosheets, and the average depth between peak and valley (*R<sub>z</sub>*) of the nanosheets was determined from the AFM height profile. X-ray photoelectron spectroscopy (XPS; ESCALAB 250Xi, Thermo Fisher Scientific, Waltham, MA, USA, electron spectrometer using Al K $\alpha$ -radiation) was conducted to determine the components and binding energies of MoS<sub>2</sub> film. Nano measurer software (Nano measurer 1.2.5, Jie Xu, Fudan University, Shanghai, China) was used to measure and calculate the average length and area density of the nanosheets.

HER tests were carried out to evaluate the catalytic performance efficiency of the as-prepared vertically standing MoS<sub>2</sub> nanosheets. All of the electrochemical measurements were performed in a 0.5 M H<sub>2</sub>SO<sub>4</sub> solution by using a three-electrode setup on an electrochemical workstation (CHI660A, CH Instruments Inc., Austin, TX, USA), with a saturated calomel electrode (SCE) as the reference electrode, a graphite rod as the counter electrode, and vertically standing MoS<sub>2</sub> nanosheets grown on an Au substrate as working electrodes. The reference electrode was calibrated with respect to a reversible hydrogen electrode (RHE). To perform the calibration, a platinum wire was used as the working electrode to run the cyclic voltammetry (CV) at a scan rate of 1 mV/s, and the average of the two potentials at which the current is zero was considered as the thermodynamic potential. Herein,  $E(\text{RHE}) = E(\text{SCE}) + 0.274 \text{ V}$ .

### 3. Results

Firstly, characterizations of a typical MoS<sub>2</sub> nanosheet deposited at  $d = 5.5 \text{ cm}$  are displayed in Figure 2. Two Raman characteristic bands at 406 and 379 cm<sup>-1</sup> with full-width half-maximum (FWHM) values of 5.5 and 5.6 cm<sup>-1</sup> are exhibited in Figure 2a, corresponding to the A<sub>1g</sub> and E<sup>1</sup><sub>2g</sub> modes of hexagonal MoS<sub>2</sub> respectively [33–35]. A<sub>1g</sub> and E<sup>1</sup><sub>2g</sub> vibrational modes are associated with the out-of-plane vibration of sulfur atoms, and the in-plane vibration of Mo and S atoms [33–35]. The E<sup>1</sup><sub>2g</sub>/A<sub>1g</sub> ratio of vertically standing MoS<sub>2</sub> nanosheets is 0.42, while that of single-crystal bulk MoS<sub>2</sub> obtained by mechanical exfoliation is 0.71 [6]. Based on this fact, the E<sup>1</sup><sub>2g</sub>/A<sub>1g</sub> relative ratio calculated from the Raman results can be used to distinguish between basal- (>0.5) and edge-oriented (<0.5) MoS<sub>2</sub> [36–38]. Consequently, it can be inferred that MoS<sub>2</sub> grown at  $d = 5.5$  was revealed to be edge-oriented, which means there are more exposed edges in vertically standing MoS<sub>2</sub> films than in single-crystal bulk MoS<sub>2</sub>.

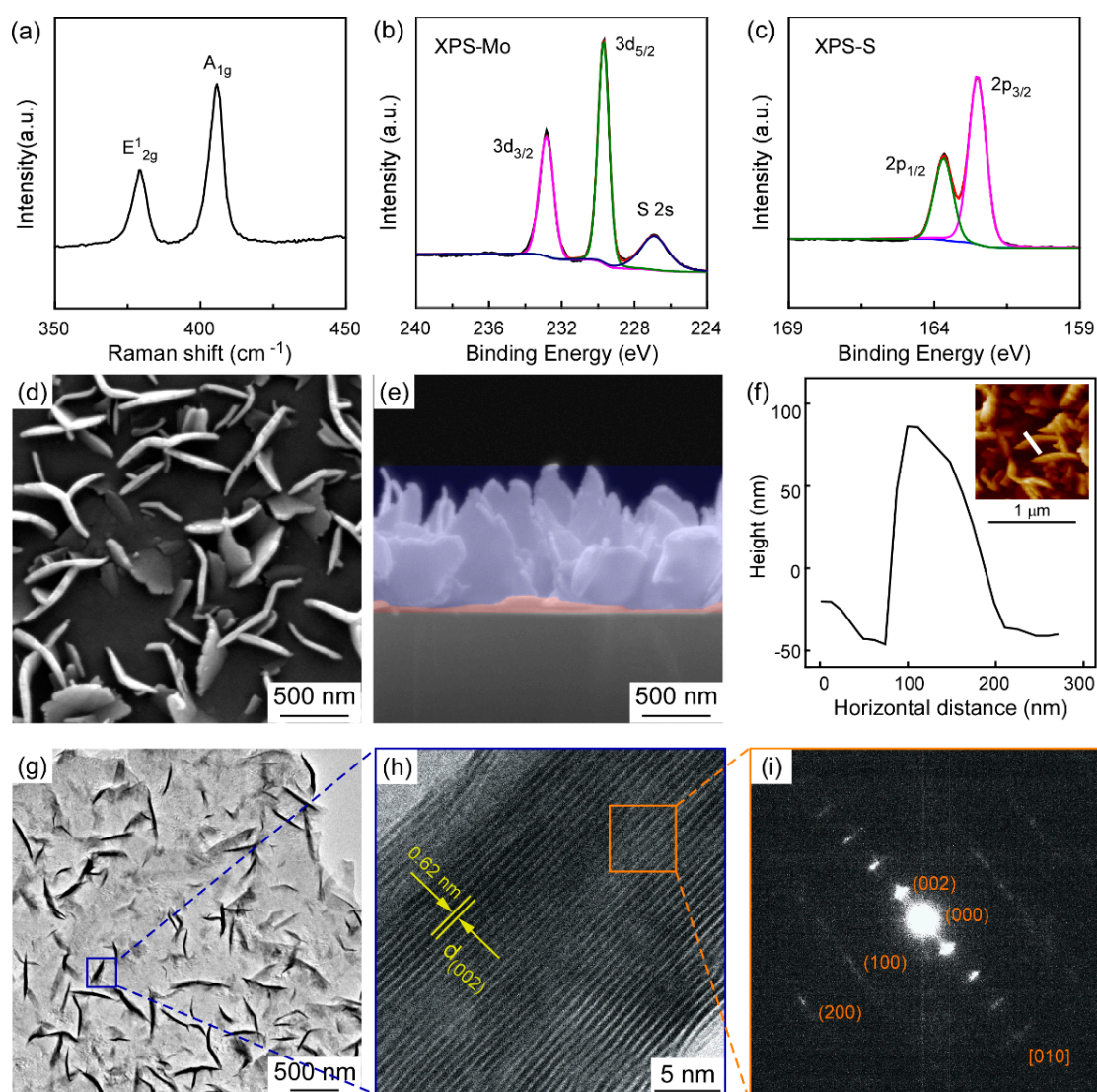


**Figure 2.** Characterizations of as-synthesized MoS<sub>2</sub> nanosheets at  $d = 5.5$  cm (distance between the precursor's outlet and substrates, denoted as  $d$ ) (a) Raman spectra; (b) XPS (X-ray photoelectron spectroscopy) of Mo  $3d$  and S  $2s$  peaks; (c) XPS spectra of S  $2p$  peak; (d) top view; and (e) cross-section FESEM (Field-emission scanning electron microscope) images of vertically standing MoS<sub>2</sub>; (f) AFM (Atomic force microscopy) height profile of single MoS<sub>2</sub> nanosheet, the insert shows the corresponding AFM image; (g) low-magnification and (h) high-magnification TEM (Transmission electron microscopy) images of MoS<sub>2</sub> nanosheets; (i) the corresponding selected area electron diffraction pattern.

Figure 2b,c shows the XPS spectra of as-grown MoS<sub>2</sub> film for Mo  $3d$  and S  $2p$  binding energies respectively. Mo  $3d$  spectra peaks [39] at two binding energies of 229.87 and 223.07 eV, corresponding to  $3d_{5/2}$  and  $3d_{3/2}$  of Mo<sup>4+</sup>. S  $2p$  [40,41] exhibits two characteristic peak positions at binding energies of 162.7 eV and 163.8 eV, which are attributed to spin-orbit  $2p_{3/2}$  and  $2p_{1/2}$  of S<sup>2-</sup> respectively. Top view and cross-section FESEM images of vertically standing MoS<sub>2</sub> are presented in Figure 2d,e. MoS<sub>2</sub> films consist of two parts (see Figure 2e): The part marked with red shadow is determined to be basal-oriented MoS<sub>2</sub> film, while the upper part marked in blue is nanosheets standing upright, which proves that the MoS<sub>2</sub> nanosheets were vertically grown on the substrate. Figure 2f shows the AFM height profile of a single MoS<sub>2</sub> nanosheet, indicating that the height of the single sheet is about 150 nm (from peak to valley).

TEM measurements were carried out in order to further characterize the crystal structure of the vertically standing MoS<sub>2</sub> nanosheets. A sample was prepared by scraping the MoS<sub>2</sub> nanosheets from the substrate, after which it was dissolved in alcohol, and the solution was dropped on a TEM grid. Figure 2g shows the low-magnification image of MoS<sub>2</sub> nanosheets, containing plentiful vertically standing nanosheets (darker part). Figure 2h records the high-magnification TEM image of the square marked in Figure 2g, which is the vertically standing MoS<sub>2</sub> nanosheets. As shown in Figure 2h, a layered structure of MoS<sub>2</sub> sheets, with a distance of 0.062 nm between two MoS<sub>2</sub> layers was obtained, suggesting that the crystal's orientation is (002) direction [7,24,38]. It can be determined that the stacking number of MoS<sub>2</sub> nanosheets is 46-layer (Figure 2h), while the stacking number of nanosheets presented in Figure 2g is in the range of 6-50 layers. Figure 2i shows the corresponding selected area electron diffraction (SAED) pattern of the square marked in Figure 2h. Regularly arranged diffraction spots are indexed as a crystal face of (002) and (100) respectively, indicating a [010] zone axis and a hexagonal crystal structure of 2H-MoS<sub>2</sub>.

Currently, out of the extensive growth mechanisms for vertically standing MoS<sub>2</sub> nanosheets proposed in the literature, the most acceptable mechanism is the so-called extrusion growth model, which demonstrates that the growth of edge-oriented MoS<sub>2</sub> nanosheets occurs after the formation of a basal-oriented structure [6]. This growth model speculates that the basal-oriented multiple MoS<sub>2</sub> layers are separately formed on the substrate surface, after which these layers reach a critical thickness, and form thick island-shaped films. Given increasing growth time, isolated thick films will become large enough to connect with each other; at this point, the edge of these island-shaped MoS<sub>2</sub> layers tend to stand up due to the extrusion between adjacent basal-oriented planes, thus producing edge-oriented MoS<sub>2</sub> nanosheets.

Based on our experiment results, a thin flat layer can be clearly observed from a cross-section image (Figure 2e), which corresponds to the basal-oriented MoS<sub>2</sub> layer. Furthermore, a few of the MoS<sub>2</sub> slabs were not vertically aligned, but rather tilted on the base surface (see Figure 2d), which could be ascribed to the asymmetrical extrusion effect. Briefly, the observation of these basal-oriented layers and tilted slabs offers direct evidence of the formation of vertically standing MoS<sub>2</sub> nanosheets, fully consistent with the proposed extrusion growth model.

The XRD and Raman results of MoS<sub>2</sub> nanosheets are presented in Figure 3. A strong sharp (002) diffraction peak is observed at  $2\theta = 14.5^\circ$ , and higher order peaks (004), (006), and (008) of MoS<sub>2</sub> have also appeared. All of these peaks can be indexed as the pure hexagonal MoS<sub>2</sub> phase with lattice constants of  $a = 3.161 \text{ \AA}$  and  $c = 12.299 \text{ \AA}$  (PDF No. 37-1942), as no diffraction peaks from impurities are observed in the XRD pattern. Figure 3c depicts the variation in FWHM value of the (002) diffraction peak. As  $d$  increases, the FWHM value of this peak decreases at first, and then increases, showing a minimum value of FWHM at  $d = 7.5 \text{ cm}$ , implying a better crystallinity in (002) direction. Two distinctive Raman peaks,  $E_{2g}^1$  ( $\sim 379 \text{ cm}^{-1}$ ) and  $A_{1g}$  ( $\sim 405 \text{ cm}^{-1}$ ), of MoS<sub>2</sub> are presented in Figure 3b. The FWHM value of  $E_{2g}^1$  peaks can be used as an indicator for MoS<sub>2</sub> crystalline quality [42], which is summarized in Figure 3c, and exhibits the same tendency as the value of XRD peaks, showing however a lowest value at  $d = 5.5 \text{ cm}$ . This inconsistency between XRD and Raman measurements may be attributable to the different sources of FWHM value. Furthermore, the  $E_{2g}^1/A_{1g}$  ratios of vertically standing MoS<sub>2</sub> nanosheets at  $d$  from 3.5 to 13.5 cm are all less than 0.5, and the values are 0.41, 0.42, 0.42, 0.41, 0.39, 0.40 respectively, indicating that deposited MoS<sub>2</sub> layers are edge-oriented. Additionally, the gap between  $E_{2g}^1$  and  $A_{1g}$  modes ranges from 25.3 to 26.9  $\text{cm}^{-1}$ , indicating that the stacking number of MoS<sub>2</sub> is 6-layer or more, which refers to a bulk character instead of a thin, few-layered 2D film [32]. This result was consistent with the TEM observation in Figure 2g.

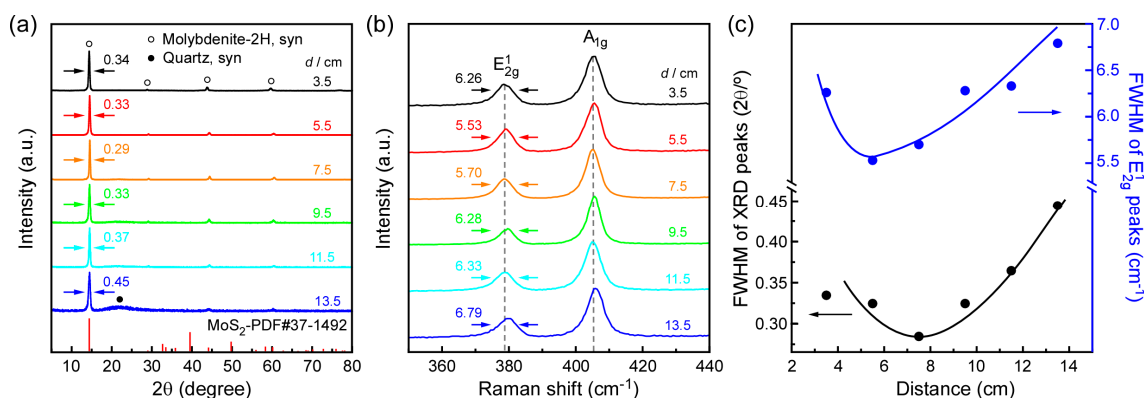


**Figure 3.** (a) XRD spectra and (c) the corresponding FWHM of (002) peak, (b) Raman spectra (c) the corresponding FWHM of  $E_{12g}^1$  peak.

The growth characteristics of MoS<sub>2</sub> deposited at different spatial locations are summarized in Figure 4. MoS<sub>2</sub> nanosheets did not lay flat on the surface of the substrate, but rather appeared to stand erect with different angles, undergoing drastic morphological changes in shape, size, density, and texture. Firstly, from the FESEM and AFM images shown in Figure 4a,b, with the increasing  $d$ , the morphology of MoS<sub>2</sub> changed from vertically standing nanosheets ( $d \leq 9.5$  cm) into nanoparticles ( $d \geq 11.5$  cm). Secondly, the average length of MoS<sub>2</sub> nanosheets calculated by Nano measurer software first increases, and then decreases. MoS<sub>2</sub> grown at  $d = 5.5$  cm indicated the largest average length, which can reach a maximum of up to 440 nm. In comparison, the area density of MoS<sub>2</sub> showed the lowest value where the MoS<sub>2</sub> sheets had the largest average length. Thirdly, although the MoS<sub>2</sub> prepared at  $d$  in the range of 5.5–9.5 stood vertically on the quartz substrate, nanosheets with three different textures, i.e., three-petal-shaped ( $d = 5.5$  cm), leaf-shaped ( $d = 7.5$  cm), and triangle-shaped ( $d = 9.5$  cm), were observed respectively. The average depth between peak and valley ( $R_z$ ) is closely related to the MoS<sub>2</sub> nanostructure, and can be explained by the average height of the nanosheets. The  $R_z$  value of MoS<sub>2</sub> shows the highest value at  $d = 5.5$  cm, leading to a maximum of 162 nm. Based on the above results, it can be concluded that sparsely distributed MoS<sub>2</sub> with a lower area density is beneficial to the growth of large size MoS<sub>2</sub> nanosheets, and contributes to a higher vertically standing structure.

A typical three-electrode device for HER test was carried out to evaluate the catalytic activity. Vertically standing MoS<sub>2</sub> nanosheets were grown on Au substrates by using the same procedure as previously described on the quartz substrate. Figure 5a–d demonstrates the typical cathodic polarization curves and corresponding Tafel plots ((a,c) for the raw data; (b,d) for the iR-corrected data). The potential for critical current density ( $j$ ) of 10 mA/cm<sup>2</sup> is considered to be a common feature of merit to evaluate the efficiency of the HER catalyst [25,43]. In Figure 5e, potential for 10 mA/cm<sup>2</sup> shows a minimum value at  $d = 5.5$  cm, indicating a good catalytic performance. An overpotential of 371 mV is needed to achieve 10 mA/cm<sup>2</sup>, while correcting the raw data for iR losses revealed an even more impressive performance (a lower overpotential of 348 mV). The Tafel slope is an inherent property of the catalyst, which is determined by the rate-limiting step of HER [7,8,44]. Figure 5f shows the Tafel slope of MoS<sub>2</sub> grown at different  $d$ : the Tafel slope is 138.9 mV/decade for raw data, and 127.8 mV/decade for iR-corrected data at  $d = 5.5$  cm. The above Tafel slope value lies in the medium region compared to previous studies, which show a wide range of Tafel slopes from 40 mV to 212 mV/decade [25,45–47]. The exchange current density  $j_0$  was determined by fitting the linear portion of the Tafel plot at a low cathodic current of the Tafel equation [15]. Based on the above results, it can be found that the most appropriate position for the growth of MoS<sub>2</sub> nanosheets was  $d = 5.5$  cm, showing the highest HER performance with the exchange current density  $j_0$  of 22.6  $\mu\text{A}/\text{cm}^2$  (19.3  $\mu\text{A}/\text{cm}^2$  for iR-corrected data)—among the medium values reported for MoS<sub>2</sub> catalysts (0.025–38.9  $\mu\text{A}/\text{cm}^2$ ) [12,48,49]. Combined with the growth characteristics and HER

performance results discussed above, it could be concluded that MoS<sub>2</sub> nanosheets with a larger average length, and higher *Rz* contributed to a better HER performance, ascribed to more exposed edge-sites in such vertically standing nanostructures.

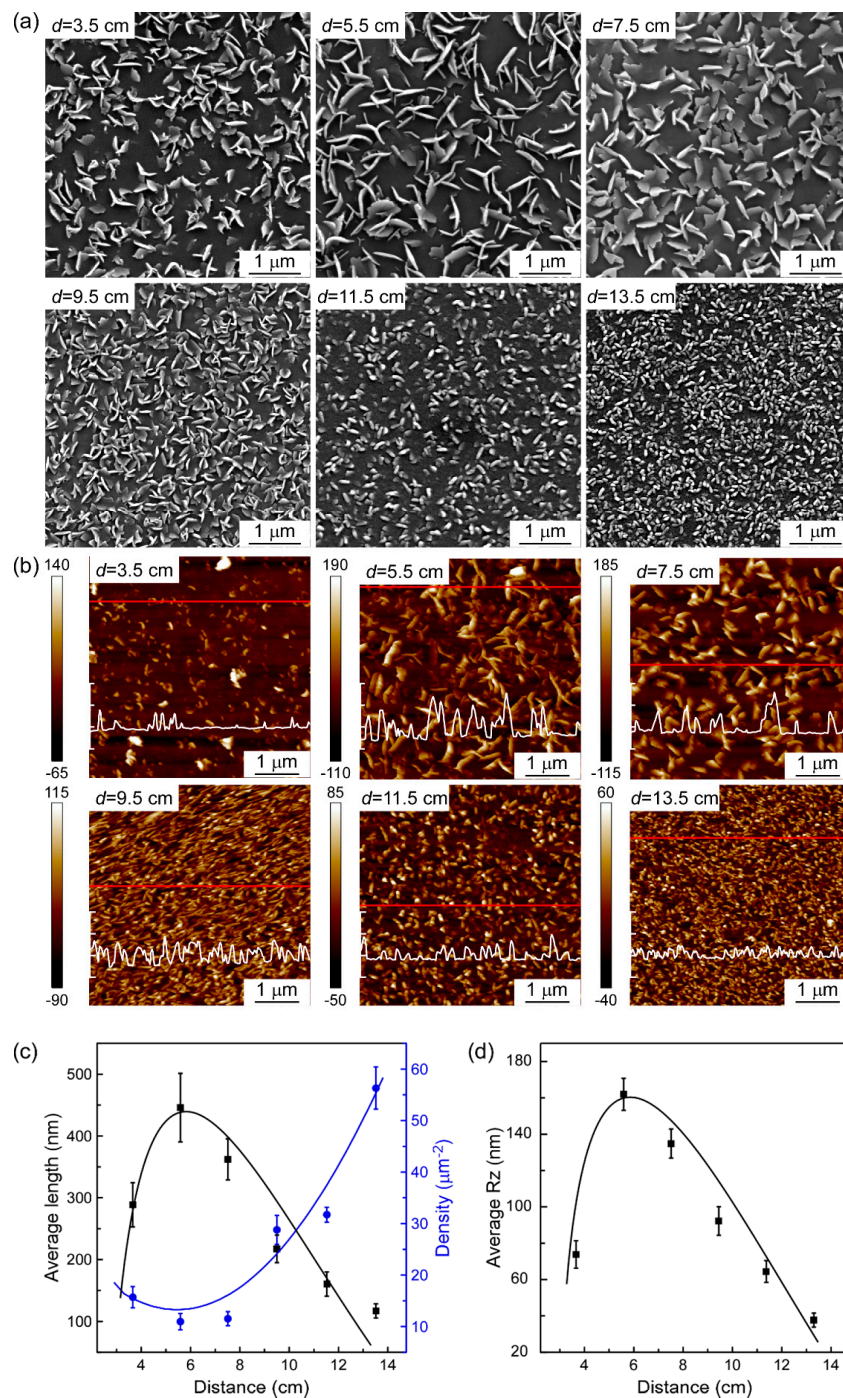


**Figure 4.** FESEM (a) and AFM (b) images of MoS<sub>2</sub> nanosheets deposited at different *d* values (3.5, 5.5, 7.5, 9.5, 11.5, 13.5 cm). The white lines overlapped on the AFM images represent the height profiles for the red lines, the scale bar is 100 nm for each interval; (c) Effect of *d* on the average length and area density (which are calculated from measured statistics of single sheet lengths and numbers by Nano measurer software) of the nanosheets. (d) Effect of *d* on average depth between peak and valley (*Rz*).

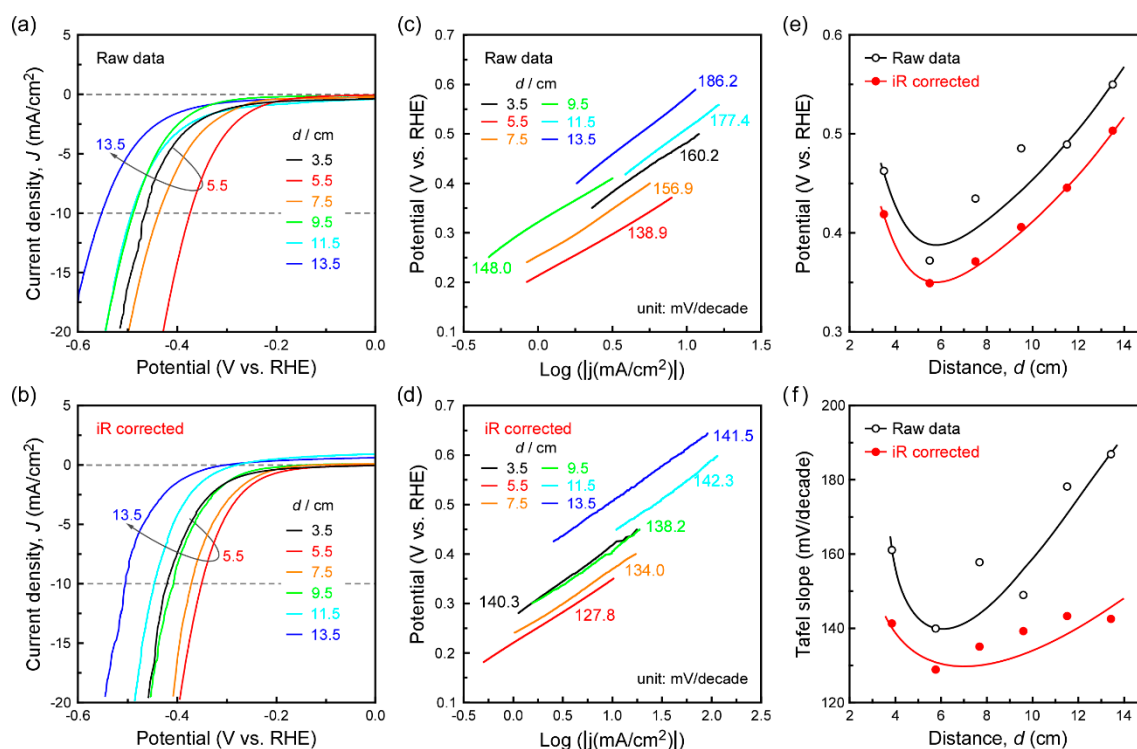


**Figure 5.** Electrochemical characterization of vertically standing MoS<sub>2</sub> nanosheets grown on Au foils at different  $d$ . Polarization curves of raw data (a) and iR-corrected data (b); corresponding Tafel plots of raw data (c) and iR-corrected data (d); potential value to achieve  $-10 \text{ mA/cm}^2$  (e) and Tafel slope (f) at different  $d$ .

#### 4. Conclusions

Vertically standing MoS<sub>2</sub> nanosheets were synthesized by the CVD method with an unconventional combination of molybdenum hexacarbonyl (Mo(CO)<sub>6</sub>) and 1,2-ethanedithiol (C<sub>2</sub>H<sub>6</sub>S<sub>2</sub>) precursors. Spatial location (i.e., the distance between precursor's outlet and the substrates, denoted as  $d$ ) played an important role in the growth characteristics of MoS<sub>2</sub>. XRD patterns and Raman indicated that 2H-MoS<sub>2</sub> with good crystallinity in (002) direction was obtained, and the FWHM value of (002) diffraction and E<sup>1</sup><sub>2g</sub> peaks reached the minimum value at  $d = 5.5 \text{ cm}$ , implying the highest crystallinity. Similarly, MoS<sub>2</sub> nanosheets grown at this location possessed the largest average length, highest  $R_z$ , and lowest area density. The vertically standing structure of edge-oriented MoS<sub>2</sub> originated from the extrusion between adjacent basal planes. Electrochemical characterization displayed that MoS<sub>2</sub> nanosheets with a larger average length and a higher  $R_z$  contributed to a better HER performance. To conclude, the most appropriate substrate spatial location is considered to be  $d = 5.5 \text{ cm}$ , where the as-deposited vertically standing MoS<sub>2</sub> nanosheets exhibited the largest average length of 440 nm, and the highest  $R_z$  of 162 nm. This contributed to a better HER performance, leading to a respective Tafel slope and exchange current density of 138.9 mV/decade and 22.6  $\mu\text{A/cm}^2$  for raw data (127.8 mV/decade and 19.3  $\mu\text{A/cm}^2$  for iR-corrected data).

**Acknowledgments:** This work was supported by National Natural Science Foundation of China, No. 51372188, No. 51521001 and the 111 Project (B13035). This research was also supported by the International Science & Technology Cooperation Program of China (2014DFA53090), the Natural Science Foundation of Hubei Province, China (2016CFA006), the Fundamental Research Funds for the Central Universities (WUT: 2017II43GX, 2017III032, 2017-YB-004, 2018 III 016), and Science Challenge Project (No. TZ2016001).

**Author Contributions:** Rong Tu, Meijun Yang, Qizhong Li conceived and designed the experiments; Jiajia Liu and Karla Hernondez performed the experiments; Song Zhang and Jiajia Liu analyzed the data; Ji Shi, Haiwen Li, Lianmeng Zhang and Takashi Goto contributed reagents/materials/analysis tools; Song Zhang and Jiajia Liu wrote the paper.

**Conflicts of Interest:** There are no conflicts to declare.

## References

1. Ji, Q.; Zhang, Y.; Zhang, Y.; Liu, Z. Chemical vapour deposition of group-VIB metal dichalcogenide monolayers: Engineered substrates from amorphous to single crystalline. *Chem. Soc. Rev.* **2015**, *44*, 2587–2602. [[CrossRef](#)] [[PubMed](#)]
2. Remskar, M.; Mrzel, A.; Skraba, Z.; Jesih, A.; Ceh, M.; Demšar, J.; Stadelmann, P.; Lévy, F.; Mihailovic, D. Self-assembly of subnanometer-diameter single-wall MoS<sub>2</sub> nanotubes. *Science* **2001**, *292*, 479–481. [[CrossRef](#)] [[PubMed](#)]
3. Li, Q.; Walter, E.C.; van der Veer, W.E.; Murray, B.J.; Newberg, J.T.; Bohannon, E.W.; Switzer, J.A.; Hemminger, J.C.; Penner, R.M. Molybdenum disulfide nanowires and nanoribbons by electrochemical/chemical synthesis. *J. Chem. Phys. B* **2005**, *109*, 3169–3182. [[CrossRef](#)] [[PubMed](#)]
4. Lv, R.; Robinson, J.A.; Schaak, R.E.; Sun, D.; Sun, Y.; Mallouk, T.E.; Terrones, M. Transition metal dichalcogenides and beyond: Synthesis, properties, and applications of single- and few-layer nanosheets. *Acc. Chem. Res.* **2015**, *48*, 56–64. [[CrossRef](#)] [[PubMed](#)]
5. Jiang, S.; Yin, X.; Zhang, J.; Zhu, X.; Li, J.; He, M. Vertical ultrathin MoS<sub>2</sub> nanosheets on a flexible substrate as an efficient counter electrode for dye-sensitized solar cells. *Nanoscale* **2015**, *7*, 10459–10464. [[CrossRef](#)] [[PubMed](#)]
6. Li, H.; Wu, H.; Yuan, S.; Qian, H. Synthesis and characterization of vertically standing MoS<sub>2</sub> nanosheets. *Sci. Rep.* **2016**, *6*, 21171. [[CrossRef](#)] [[PubMed](#)]
7. Ling, L.; Wang, C.; Zhang, K.; Li, T.T.; Tang, L.; Li, C.W.; Wang, L.J.; Xu, Y.C.; Song, Q.J.; Yao, Y.G. Controlled growth of MoS<sub>2</sub> nanopetals and their hydrogen evolution performance. *RSC Adv.* **2016**, *6*, 18483–18489. [[CrossRef](#)]
8. Deokar, G.; Vignaud, D.; Arenal, R.; Louette, P.; Colomer, J.F. Modification of graphene oxide by laser irradiation: A new route to enhance antibacterial activity. *Nanotechnology* **2016**, *27*, 10.
9. Wang, X.; Zhang, Z.; Chen, Y.; Qu, Y.; Lai, Y.; Li, J. Morphology-controlled synthesis of MoS<sub>2</sub> nanostructures with different lithium storage properties. *J. Alloys Compd.* **2014**, *600*, 84–90. [[CrossRef](#)]
10. Teng, Y.; Zhao, H.; Zhang, Z.; Li, Z.; Xia, Q.; Zhang, Y.; Zhao, L.; Du, X.; Du, Z.; Lv, P.; et al. MoS<sub>2</sub> Nanosheets Vertically Grown on Graphene Sheets for Lithium-Ion Battery Anodes. *ACS Nano* **2016**, *10*, 8526–8535. [[CrossRef](#)] [[PubMed](#)]
11. Deokar, G.; Rajput, N.S.; Vancso, P.; Ravaux, F.; Jouiad, M.; Vignaud, D.; Cecchet, F.; Colomer, J.F. Large area growth of vertically aligned luminescent MoS<sub>2</sub> nanosheets. *Nanoscale* **2017**, *9*, 277–287. [[CrossRef](#)] [[PubMed](#)]
12. Wu, Z.; Fang, B.; Wang, Z.; Wang, C.; Liu, Z.; Liu, F.; Wang, W.; Alfantazi, A.; Wang, D.; Wilkinson, D.P. MoS<sub>2</sub> Nanosheets: A Designed Structure with High Active Site Density for the Hydrogen Evolution Reaction. *ACS Catal.* **2013**, *3*, 2101–2107. [[CrossRef](#)]
13. Chhowalla, M.; Shin, H.S.; Eda, G.; Li, L.-J.; Loh, K.P.; Zhang, H. The chemistry of two-dimensional layered transition metal dichalcogenide nanosheets. *Nat. Chem.* **2013**, *5*, 263–275. [[CrossRef](#)] [[PubMed](#)]
14. Kibsgaard, J.; Chen, Z.; Reinecke, B.N.; Jaramillo, T.F. Engineering the surface structure of MoS<sub>2</sub> to preferentially expose active edge sites for electrocatalysis. *Nat. Mater.* **2012**, *11*, 963–969. [[CrossRef](#)] [[PubMed](#)]
15. Li, S.; Wang, S.; Salamone, M.M.; Robertson, A.W.; Nayak, S.; Kim, H.; Tsang, S.C.E.; Pasta, M.; Warner, J.H. Edge-Enriched 2D MoS<sub>2</sub> Thin Films Grown by Chemical Vapor Deposition for Enhanced Catalytic Performance. *ACS Catal.* **2017**, *7*, 877–886. [[CrossRef](#)]
16. Zhang, Y.; Ji, Q.; Han, G.; Ju, J.; Shi, J.; Ma, D.; Sun, J. Dendritic, Transferable, Strictly Monolayer MoS<sub>2</sub> Flakes Synthesized on SrTiO<sub>3</sub> Single Crystals for Efficient Electrocatalytic Applications. *ACS Nano* **2014**, *8*, 8617–8624. [[CrossRef](#)] [[PubMed](#)]

17. Lukowski, M.A.; Daniel, A.S.; Meng, F.; Forticaux, A.; Li, L.; Jin, S. Enhanced Hydrogen Evolution Catalysis from Chemically Exfoliated Metallic MoS<sub>2</sub> Nanosheets. *J. Am. Chem. Soc.* **2013**, *135*, 10274–10277. [[CrossRef](#)] [[PubMed](#)]
18. Yoo, Y.; Degregorio, Z.P.; Johns, J.E. Seed Crystal Homogeneity Controls Lateral and Vertical Heteroepitaxy of Monolayer MoS<sub>2</sub> and WS<sub>2</sub>. *J. Am. Chem. Soc.* **2015**, *137*, 14281–14287. [[CrossRef](#)] [[PubMed](#)]
19. Cao, Y.; Luo, X.; Yuan, C.; Han, S.; Yu, T.; Yang, Y.; Li, Q. Morphology engineering of monolayer MoS<sub>2</sub> by adjusting chemical environment during growth. *Phys. E Low Dimens. Syst. Nanostruct.* **2015**, *74*, 292–296. [[CrossRef](#)]
20. Cao, D.; Shen, T.; Liang, P.; Chen, X.; Shu, H. Role of Chemical Potential in Flake Shape and Edge Properties of Monolayer MoS<sub>2</sub>. *J. Phys. Chem. C* **2015**, *119*, 4294–4301. [[CrossRef](#)]
21. Wang, S.S.; Rong, Y.M.; Fan, Y.; Pacios, M.; Bhaskaran, H.; He, K.; Warner, J.H. Shape Evolution of Monolayer MoS<sub>2</sub> Crystals Grown by Chemical Vapor Deposition. *Chem. Mater.* **2014**, *26*, 6371–6379. [[CrossRef](#)]
22. Cho, S.Y.; Kim, S.J.; Lee, Y.; Kim, J.S.; Jung, W.B.; Yoo, H.W.; Kim, J.; Jung, H.T. Highly Enhanced Gas Adsorption Properties in Vertically Aligned MoS<sub>2</sub> Layers. *ACS Nano* **2015**, *9*, 9314–9321. [[CrossRef](#)] [[PubMed](#)]
23. Wang, H.; Tsai, C.; Kong, D.; Chan, K.; Abild-pedersen, F.; Nørskov, J.K.; Cui, Y. Transition-metal doped edge sites in vertically aligned MoS<sub>2</sub> catalysts for enhanced hydrogen evolution. *Nano Res.* **2015**, *8*, 566–575. [[CrossRef](#)]
24. Zhou, Y.; Liu, Y.; Zhao, W.; Xie, F.; Xu, R.; Li, B.; Zhou, X.; Shen, H. Growth of vertically aligned MoS<sub>2</sub> nanosheets on a Ti substrate through a self-supported bonding interface for high-performance lithium-ion batteries: A general approach. *J. Mater. Chem. A* **2016**, *4*, 5932–5941. [[CrossRef](#)]
25. Bhimanapati, G.R.; Hankins, T.; Vila, R.A.; Yu, L.; Fuller, I.; Terrones, M.; Robinson, J.A. Growth and Tunable Surface Wettability of Vertical MoS<sub>2</sub> Layers for Improved Hydrogen Evolution Reactions. *ACS Appl. Mater. Interfaces* **2016**, *8*, 22190–22195. [[CrossRef](#)] [[PubMed](#)]
26. Shokhen, V.; Miroshnikov, Y.; Gershinsky, G.; Gotlib, N.; Stern, C.; Naveh, D.; Zitoun, D.; Ilan, B.; Bina, A.M.; Gan, R. On the impact of Vertical Alignment of MoS<sub>2</sub> for Efficient Lithium Storage. *Sci. Rep.* **2017**, *7*, 3280. [[CrossRef](#)] [[PubMed](#)]
27. Perkgoz, N.K.; Bay, M. Investigation of Single-Wall MoS<sub>2</sub> Monolayer Flakes Grown by Chemical Vapor Deposition. *Nano Micro Lett.* **2016**, *8*, 70–79. [[CrossRef](#)]
28. Zhang, Y.; Zhang, Y.; Ji, Q.; Ju, J.; Yuan, H.; Shi, J.; Gao, T.; Ma, D.; Liu, M.; Chen, Y.; et al. Controlled Growth of High-Quality Monolayer WS<sub>2</sub> Layers on Sapphire and Imaging Its Grain Boundary. *ACS Nano* **2013**, *7*, 8963–8971. [[CrossRef](#)] [[PubMed](#)]
29. Lin, Z.; Zhao, Y.; Zhou, C.; Zhong, R.; Wang, X.; Tsang, Y.H.; Chai, Y. Controllable Growth of Large-Size Crystalline MoS<sub>2</sub> and Resist-Free Transfer Assisted with a Cu Thin Film. *Sci. Rep.* **2016**, *5*, 18596. [[CrossRef](#)] [[PubMed](#)]
30. Duphil, D.; Bastide, S.; Lévy-Clément, C. Chemical Synthesis of Molybdenum Disulfide Nanoparticles in an Organic Solution. *J. Mater. Chem.* **2002**, *12*, 2430–2432. [[CrossRef](#)]
31. Tao, H.; Yanagisawa, K.; Zhang, C.; Ueda, T.; Onda, A.; Li, N.; Shou, T. Synthesis and Growth Mechanism of Monodispersed MoS<sub>2</sub> Sheets/Carbon Microspheres. *CrystEngComm* **2012**, *14*, 3027. [[CrossRef](#)]
32. Kumar, V.K.; Dhar, S.; Choudhury, T.H.; Shivashankar, S.A.; Raghavan, S. A predictive approach to CVD of crystalline layers of TMDs: The case of MoS<sub>2</sub>. *Nanoscale* **2015**, *7*, 7802–7810. [[CrossRef](#)] [[PubMed](#)]
33. Zhang, X.; Han, W.P.; Wu, J.B.; Milana, S.; Lu, Y.; Li, Q.Q.; Ferrari, A.C.; Tan, P.H. Raman spectroscopy of shear and layer breathing modes in multilayer MoS<sub>2</sub>. *Phys. Rev. B* **2013**, *87*, 115413. [[CrossRef](#)]
34. Conley, H.J.; Wang, B.; Ziegler, J.I.; Haglund, R.F.; Pantelides, S.T.; Bolotin, K.I. Bandgap Engineering of Strained Monolayer and Bilayer MoS<sub>2</sub>. *Nano Lett.* **2013**, *13*, 3626–3630. [[CrossRef](#)] [[PubMed](#)]
35. Jeong, S.; Shin, H.-Y.; Shin, R.H.; Jo, W.; Yoon, S.; Rübhausen, M. Raman scattering studies of the lattice dynamics in layered MoS<sub>2</sub>. *J. Korean Phys. Soc.* **2015**, *66*, 1575–1580. [[CrossRef](#)]
36. Yang, Y.; Fei, H.; Ruan, G.; Xiang, C.; Tour, J.M. Edge-oriented MoS<sub>2</sub> nanoporous films as flexible electrodes for hydrogen evolution reactions and supercapacitor devices. *Adv. Mater.* **2014**, *26*, 8163–8168. [[CrossRef](#)] [[PubMed](#)]
37. Tan, S.M.; Ambrosi, A.; Sofer, Z.; Huber, Š.; Sedmidubský, D.; Pumera, M. Pristine Basal- and Edge-Plane-Oriented Molybdenite MoS<sub>2</sub> Exhibiting Highly Anisotropic Properties. *Chem. A Eur. J.* **2015**, *21*, 7170–7178. [[CrossRef](#)] [[PubMed](#)]

38. Fei, L.; Lei, S.; Zhang, W.B.; Lu, W.; Lin, Z.; Lam, C.H.; Chai, Y.; Wang, Y. Direct TEM observations of growth mechanisms of two-dimensional MoS<sub>2</sub> flakes. *Nat. Commun.* **2016**, *7*, 12206. [[CrossRef](#)] [[PubMed](#)]
39. Wang, J.; Chen, L.; Lu, W.; Zeng, M.; Tan, L.; Ren, F.; Jiang, C.; Fu, L. Direct growth of molybdenum disulfide on arbitrary insulating surfaces by chemical vapor deposition. *RSC Adv.* **2015**, *5*, 4364–4367. [[CrossRef](#)]
40. Choi, Y.; Lee, J.; Parija, A.; Cho, J.; Verkhoturov, S.V.; Al-hashimi, M.; Fang, L.; Banerjee, S. An in Situ Sulfidation Approach for the Integration of MoS<sub>2</sub> Nanosheets on Carbon Fiber Paper and the Modulation of Its Electrocatalytic Activity by Interfacing with nC<sub>60</sub>. *ACS Catal.* **2016**, *6*, 6246–6254. [[CrossRef](#)]
41. Mos, R.L.; Fullerene-like, W.S.I. Atmospheric Pressure Chemical Vapor Deposition: An Alternative Route to Large-Scale MoS<sub>2</sub> and WS<sub>2</sub> Inorganic Fullerene-like Nanostructures and Nanoflowers. *Chem. A Eur. J.* **2004**, *10*, 6163–6171.
42. Yu, Y.; Li, C.; Liu, Y.; Su, L.; Zhang, Y.; Cao, L. Controlled Scalable Synthesis of Uniform, High-Quality Monolayer and Few-layer MoS<sub>2</sub> Films. *Sci. Rep.* **2013**, *3*, 1866. [[CrossRef](#)] [[PubMed](#)]
43. Benck, J.D.; Hellstern, T.R.; Kibsgaard, J.; Chakthranont, P.; Jaramillo, T.F. Catalyzing the hydrogen evolution reaction (HER) with molybdenum sulfide nanomaterials. *ACS Catal.* **2014**, *4*, 3957–3971. [[CrossRef](#)]
44. Conway, B.E.; Tilak, B.V. Interfacial processes involving electrocatalytic evolution and oxidation of H<sub>2</sub>, and the role of chemisorbed H. *Electrochim. Acta* **2002**, *47*, 3571–3594. [[CrossRef](#)]
45. Tao, L.; Duan, X.; Wang, C.; Duan, X.; Wang, S. Plasma-engineered MoS<sub>2</sub> thin-film as an efficient electrocatalyst for hydrogen evolution reaction. *Chem. Commun.* **2015**, *51*, 7470–7473. [[CrossRef](#)] [[PubMed](#)]
46. Ji, Q.; Zhang, Y.; Shi, J.; Sun, J.; Zhang, Y.; Liu, Z. Morphological Engineering of CVD-Grown Transition Metal Dichalcogenides for Efficient Electrochemical Hydrogen Evolution. *Adv. Mater.* **2016**, *28*, 6207–6212. [[CrossRef](#)] [[PubMed](#)]
47. Wang, H.; Zhang, Q.; Yao, H.; Liang, Z.; Lee, H.W.; Hsu, P.C.; Zheng, G.; Cui, Y. High Electrochemical Selectivity of Edge versus Terrace Sites in Two-Dimensional Layered MoS<sub>2</sub> Materials. *Nano Lett.* **2014**, *14*, 7138–7144. [[CrossRef](#)] [[PubMed](#)]
48. Shin, S.; Jin, Z.; Kwon, D.H.; Bose, R.; Min, Y.S. High Turnover Frequency of Hydrogen Evolution Reaction on Amorphous MoS<sub>2</sub> Thin Film Directly Grown by Atomic Layer Deposition. *Langmuir* **2015**, *31*, 1196–1202. [[CrossRef](#)] [[PubMed](#)]
49. Yan, Y.; Xia, B.; Li, N.; Xu, Z.; Fisher, A.; Wang, X.J. Vertically oriented MoS<sub>2</sub> and WS<sub>2</sub> nanosheets directly grown on carbon cloth as efficient and stable 3-dimensional hydrogen-evolving cathodes. *Mater. Chem. A* **2015**, *3*, 131–135. [[CrossRef](#)]



© 2018 by the authors. Licensee MDPI, Basel, Switzerland. This article is an open access article distributed under the terms and conditions of the Creative Commons Attribution (CC BY) license (<http://creativecommons.org/licenses/by/4.0/>).